

PVP2021-62207

EXPLICIT FINITE ELEMENT FATIGUE CRACK GROWTH ANALYSIS OF AN INSTRUMENTATION RING UNDER THERMAL TRANSIENT LOADING

Joshua B. B. Selling, James E. Holliday, Thomas M. Damiani

Naval Nuclear Laboratory
 PO Box 79
 West Mifflin, PA 15122-0079

ABSTRACT

ASME PVP conference papers from 2007 and 2008 (References [1] and [2]) discuss fatigue analyses related to 304 stainless steel instrumentation spacer rings (rings) that had cracked while installed in a thermal fatigue test loop. The rings contain circular radial penetrations extending through the ring that allow access for instrumentation probes to monitor the fluid temperature and pressure. Routine inspection of the test loop revealed actively growing cracks in each port that appeared to start near the inner diameter (ID) of the ring. In this work, three-dimensional finite element analysis (FEA) thermal and fully-elastic structural Abaqus models were made from the available test measurements. The commercial crack modeling software, Franc3D, was used to complete an M-integral based fatigue crack growth (FCG) analysis. An assumed initial crack was inserted in a single port of interest near the ID of the FEA model. The crack was explicitly grown in an automated fashion over iterative growth steps. The explicit FCG analysis was able to match the directional path and final flaw size seen in the destructive evaluation metallographic images of the rings with the assumed input parameters exceptionally well, including shifting directions and splitting the crack without need of user input. The results of this work indicate that an explicit FCG analysis is feasible for a non-trivial thermal-structural problem.

Keywords: Abaqus, Franc3D, finite element analysis, FEA, explicit, fatigue, crack, growth, analysis, thermal, transient, structural, test loop

NOMENCLATURE

E	Young's Modulus
α_m	Mean Coefficient of Thermal Expansion
C_v	Specific Heat (at Constant Volume)
ρ	Density
T	Temperature
k	Thermal Conductivity
K	Stress Intensity Factor
K_I	Mode 1 Stress Intensity Factor
K_{II}	Mode 2 Stress Intensity Factor
K_{III}	Mode 3 Stress Intensity Factor
ΔK	Stress Intensity Factor Range
ΔK_{eff}	Effective Stress Intensity Factor Range
$\Delta K_{threshold}$	Threshold Stress Intensity Factor Range
$K_{critical}$	Critical Stress Intensity Factor
$\frac{Da}{DN} = C_0 \cdot (\Delta K)^n$	General Paris Law Model expressed in $\frac{\text{inches}}{\text{cycle}}$
C_0	Paris Law Model Leading Coefficient
n	Paris Law Model ΔK Exponent
$R = \frac{K_{min}}{K_{max}}$	R ratio
t_{Rise}	Rise time expressed in seconds

1. INTRODUCTION

Structural components subjected to fatigue cycling primarily by thermally-induced stress are common in the ASME Boiler and Pressure Vessel community. As discussed in 2007 and 2008 ASME PVP conference papers (References [1] and [2]), a thermal fatigue test loop was constructed by Bechtel Bettis, Inc. (now Naval Nuclear Laboratory) to obtain thermal fatigue data on piping and piping weldments. The test loop is illustrated in Figure 1 and consists of independent hot and cold loops that connect to the piping test section. The inlet and outlet of the piping test section includes 304 stainless steel (304SS) instrumentation spacer rings (rings) (see Figure 2). The rings each have five circular radial penetrations extending through the ring to allow access for instrumentation probes (see Figure 3). One of the penetrations has a continuous diameter (pressure port) and the other four have a smaller diameter region near the inner diameter (ID) of the ring to support a thermocouple housing (thermocouple port). Routine inspection of the test loop revealed actively growing cracks in all five ports that appeared to start near the ID of the ring (see Figure 4). It was the fast cooling and heating on the ID of the rings from forced fluid flow that lead to a large gradient of thermally-induced stress in the radial direction. Cracking was more pronounced in the four thermocouple ports than in the one pressure port.

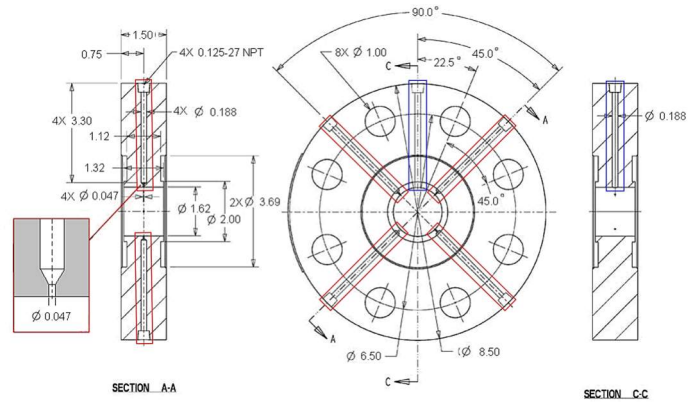


Figure 3. Instrumentation Spacer Ring Drawing.

There are five circular radial penetrations extending through the ring: four thermocouple ports (boxed in red) with a smaller diameter region near the ID of the ring and one pressure port (boxed in blue) with a continuous diameter.

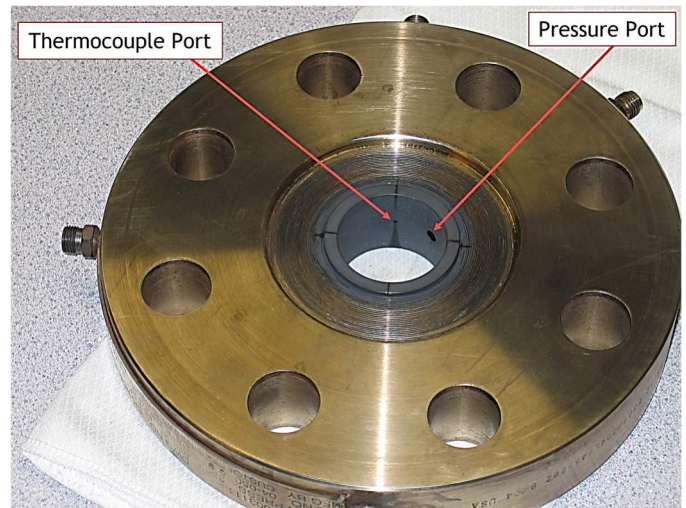


Figure 4. Cracked Instrumentation Spacer Ring.

Routine inspection of the test loop revealed actively growing cracks in all five ports that appeared to start near the ID of the ring. Cracking was more pronounced in the four thermocouple ports than in the one pressure port. A ring after 34,000 cycles is pictured.

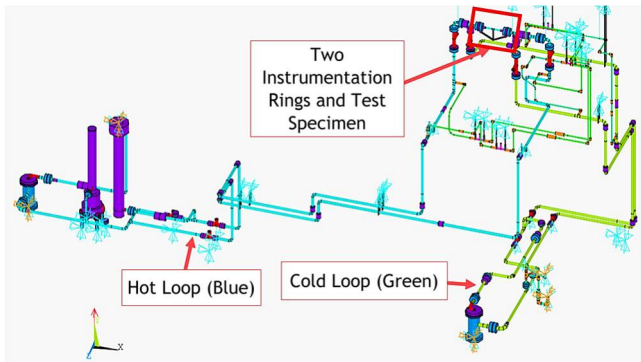


Figure 1. Thermal Fatigue Test Loop.

The loop consists of independent hot and cold loops that connect to the piping test section. The piping test section consists of two instrumentation spacer rings and one test specimen (see Figure 2).

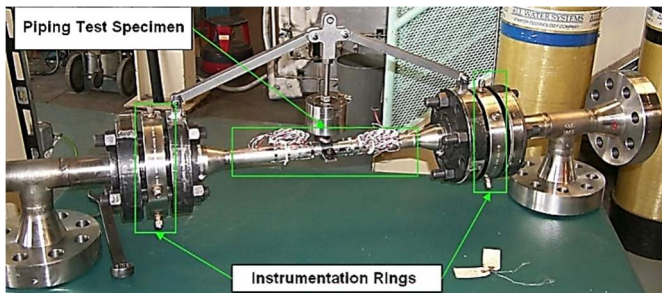


Figure 2. Piping Test Section.

The piping test section includes two instrumentation spacer rings and one test specimen.

2. MATERIALS AND METHODS

2.1. Testing and Observed Cracks

The test loop fluid was cycled from a hot fluid temperature of 500 °F to a cold fluid temperature of 100 °F and back to 500 °F, with a hold time between each temperature to establish thermal equilibrium. The pressure varied between 1900 psi to 1000 psi. Fluid flow rate varied from 60 gallons per minute (gpm) to 40 gpm during the cool down phase of the cycle, and back up to 60 gpm during the heat up phase of the cycle. One transient cycle was about 200 seconds. In this analysis, the representative transient cycle considered was 206 seconds. Representative plots of fluid temperature (at the top of the flow path, the bottom of the flow path, and the average fluid temperature), fluid pressure, and fluid flow (both the hot loop and cold loop flow rates are shown as the flow through the piping test section was not actively monitored) for 2.5 cycles are shown in Figures 5, 6, and 7, respectively. Additional details about the test loop are in References [1] and [2].

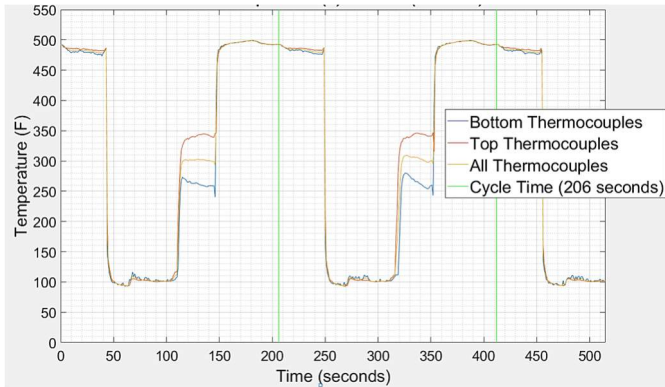


Figure 5. Fluid Temperature (°F) vs. Time (s) for 2.5 cycles (1 cycle = 206 seconds).

Temperature was monitored at the top of the flow path (two thermocouples) and the bottom of the flow path (two thermocouples). The average of all four thermocouples is also plotted.

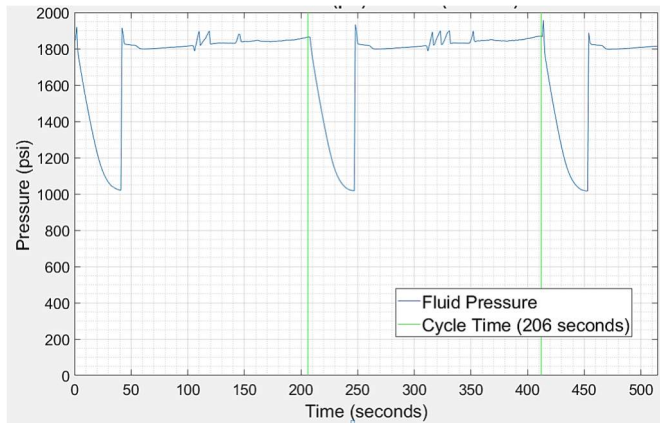


Figure 6. Fluid Pressure (psi) vs. Time (s) for 2.5 cycles (1 cycle = 206 seconds)

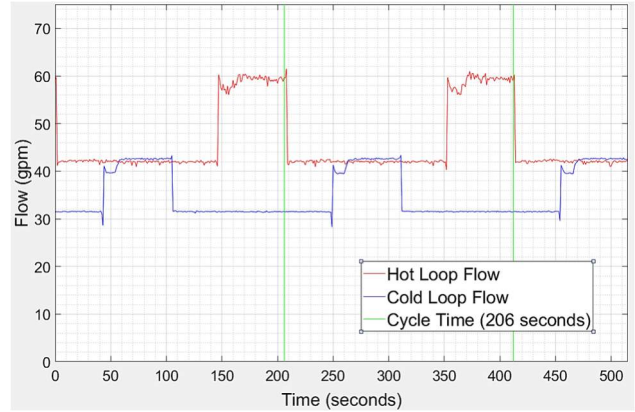


Figure 7. Fluid Flow (gpm) vs. Time (s) for 2.5 cycles (1 cycle = 206 seconds).

The indicated flow is the hot loop flow and the cold loop flow as the flow through the piping test section was not actively monitored.

There are four 304SS rings (two sets) that have gone through testing and measurement data of the surface crack length is available for 38,000 and 20,971 transient cycles, respectively. The measurements were done visually with no magnification. The surface crack length was visually observed to grow in the axial direction (i.e., aligned in the direction of the flow) and then once reaching the edge of the ring, continued to grow in the radial direction. Only one edge of the crack could be visually observed as the other edge of the crack was within the port. Based on the destructive evaluation (DE) metallographic images and the crack striation lines, the crack front changed shape and grew bi-axially (radially and axially) through the thickness of the ring. As the four thermocouple ports experienced more pronounced cracking than the one pressure port, a thermocouple port was the subject of this analysis. A DE metallographic image of a thermocouple port of one of the rings after 38,000 cycles is provided in Figure 8.

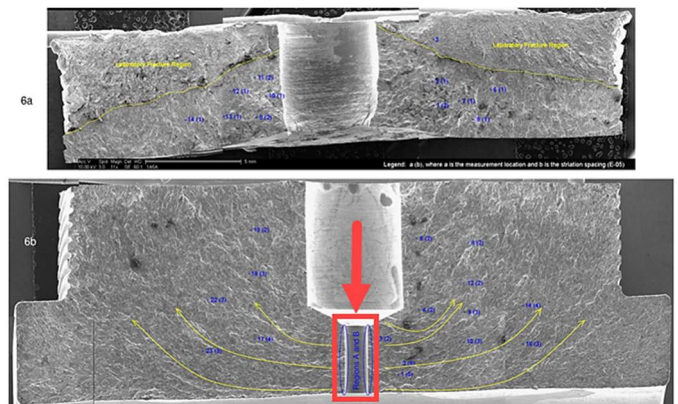


Figure 8. Destructive Evaluation Scanning Electron Microscope Image of Cracked Thermocouple Port.

Crack growth surfaces from 38,000 cycles is shown above. The upper photo and lower photo are a continuation of the same sample. Crack initiation was observed to be somewhere along the smaller diameter region (i.e., the step-down), marked by the red box.

2.2. Thermal and Structural FEA

Three-dimensional FEA models of the ring were created in a similar manner (but not identical) as was done in References [1] and [2]. A 1/8 symmetric (1/4 sweep and 1/2 thickness) geometric model that isolated the thermocouple port was developed (see Figure 9). References [1] and [2] also created a 1/8 symmetric geometric model, but located the port at the edge of model, while in this work the port was located at the center of the model. This was done to facilitate the explicit modeling of a full crack (since a port located at the edge of the model resulted in modeling only half of a crack). The 304SS material was set to have a Poisson's ratio was 0.3. The temperature dependent material properties of 304SS are listed in Table 1.

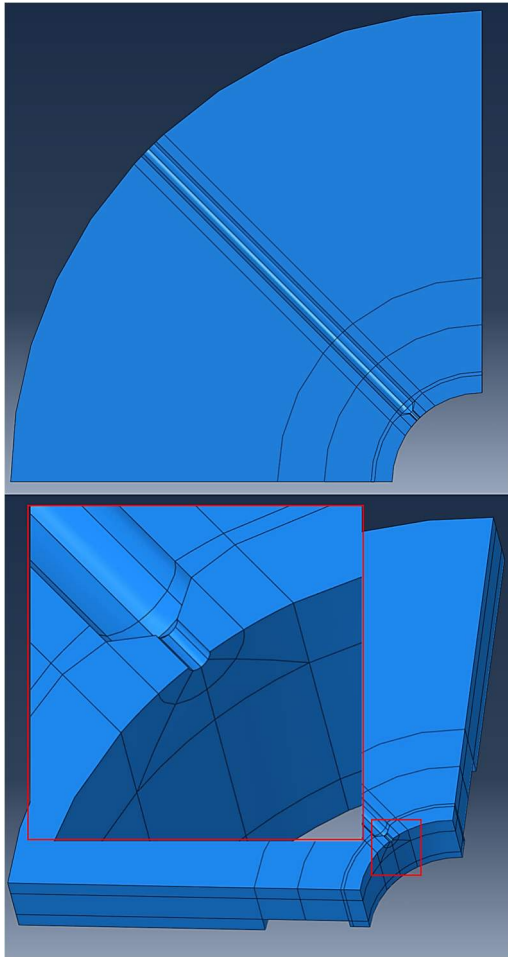


Figure 9. 1/8 Symmetric (1/4 sweep and 1/2 thickness) Geometric FEA Model with an Isolated Thermocouple Port

Table 1. Material Properties of 304SS

T	E	k	α_m
$^{\circ}F$	$10^6 \frac{lbf}{in^2}$	$10^{-4} \frac{BTU}{s \cdot inch \cdot ^{\circ}F}$	$10^{-6} \frac{in/in}{^{\circ}F}$
70	28.3	1.99074	8.7
200	27.8	2.15278	9.0
400	26.7	2.38426	9.4
600	25.5	2.59259	9.6
700	24.9	2.68519	9.7
T	C_p	ρ	
$^{\circ}F$	$\frac{BTU}{(\frac{lbf \cdot s^2}{in}) \cdot ^{\circ}F}$	$10^{-4} \frac{(\frac{lbf \cdot s^2}{in})}{in^3}$	
70	46.7166	7.51124	
200	47.8749	7.48534	
400	49.8054	7.43354	
600	51.7358	7.40764	
700	52.5080	7.38174	

First, a thermal FEA was created. Simplified datasets of the transient data seen in Figures 5, 6, and 7 were used to calculate forced convection heat transfer coefficients (HTCs). The fluid temperature was assumed to be the average fluid temperature. The fluid flow rate was assumed to be the respective loop flow rate, as the flow rate through the test specimen was not directly measured. Additionally, the fluid flow rate was converted from a volumetric flow rate to a mass flow rate. A modified Gnielinski correlation was used to calculate the HTCs, where (i) a Blasius friction factor was used, (ii) pipe length flow development was accounted for, and (iii) the fluid property variations term was neglected. The Gnielinski correlation was taken from Reference [3], Equation 10.98a (the $(Pr/Pr_w)^{0.11}$ term was neglected) and the Blasius friction factor was taken from Reference [3], Equation 9.88. The HTCs used in the thermal analysis are plotted in Figure 10.

The ID of the ring was modeled with forced convection and all other surfaces were modeled as adiabatic (see Figure 11). Natural convection during the hold periods was neglected as the forced convection HTCs during periods of forced flow were judged to be orders of magnitude larger. The thermal FEA mesh consisted of 274,340 twenty-node hexahedral elements and 1,149,118 nodes (see Figure 12).

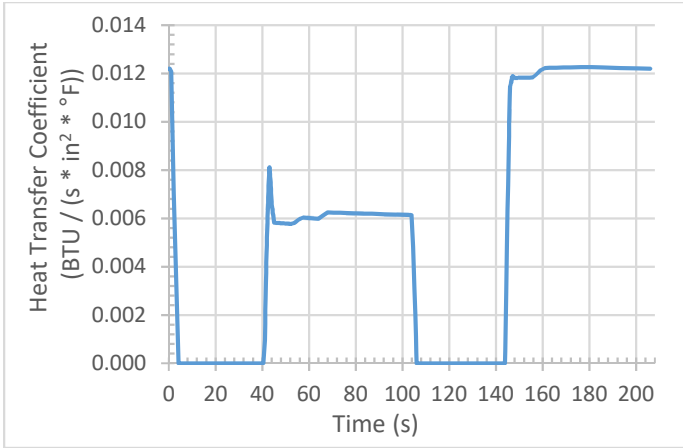


Figure 10. Thermal FEA Forced Convection HTC
 $\left(\frac{BTU}{s \cdot in^2 \cdot °F}\right)$ vs. Time (s).

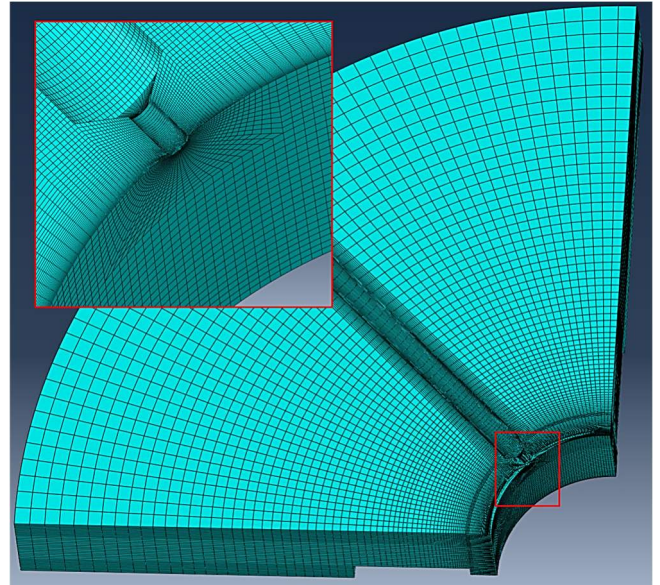


Figure 12. Thermal FEA Mesh.
 274,340 twenty-node hexahedral elements and 1,149,118 nodes.

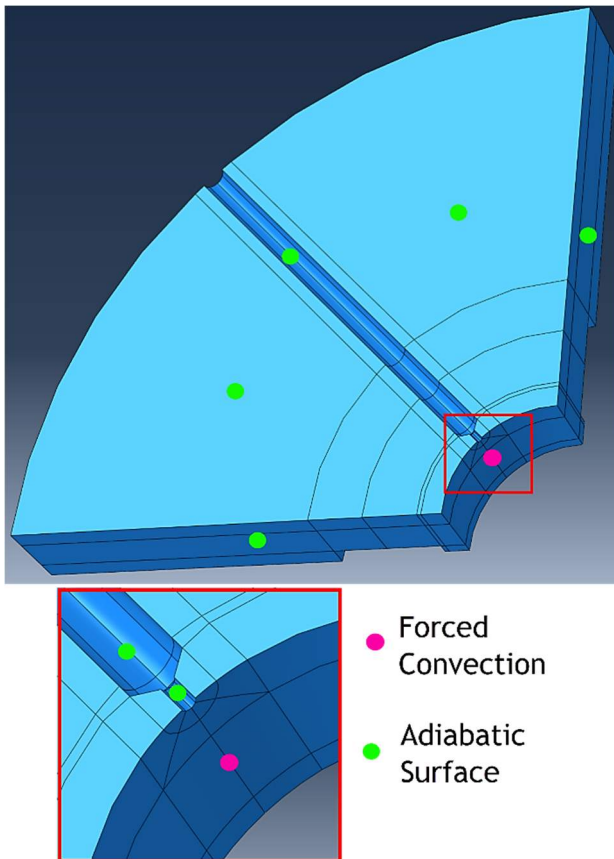


Figure 11. Thermal FEA Boundary Conditions.
 The ID of the ring was modeled with forced convection and all other surfaces were modeled as adiabatic.

Next, a structural fully-elastic FEA was created that interpolated the thermal FEA solution onto the dissimilar structural FEA mesh. The structural FEA was performed and field outputs were requested at all thermal FEA solution time points. The three planes of symmetry were modeled with zero displacement across the associated normal to the plane of symmetry (see Figure 13). Although the pressure stress is small compared to the thermal stress, for completeness the tabulated fluid pressure was used to model pressure loading along the ID of the ring and throughout the length of the port (see Figure 14). The effect of bolting on the ring was neglected. The un-cracked structural FEA mesh consisted of 29,044 twenty-node full-integration hexahedral elements and 127,476 nodes (see Figure 15). The un-cracked structural mesh is less refined than the thermal mesh as the structural mesh was solved during each crack growth step (the process is explained in Section 2.4). Additionally, the region of interest where crack initiation was assumed was re-meshed with high fidelity close to the crack during each growth step.

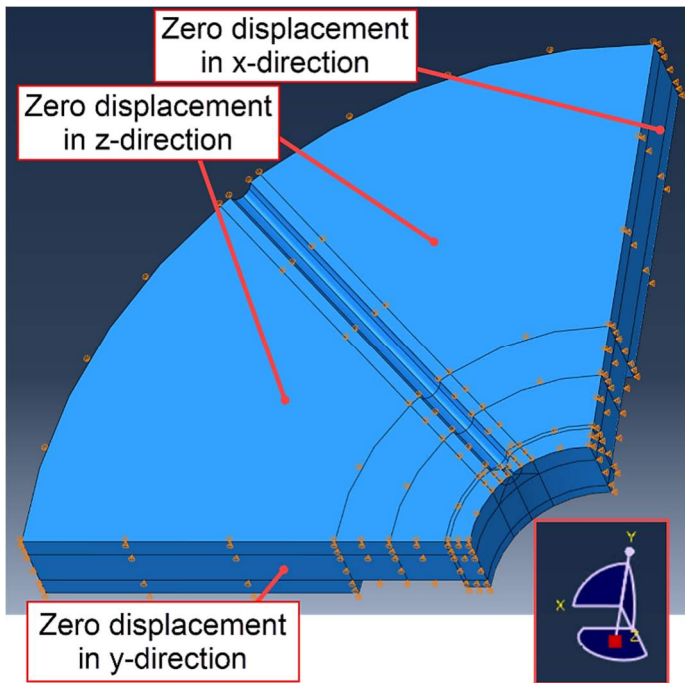


Figure 13. Structural FEA Kinematic Constraints

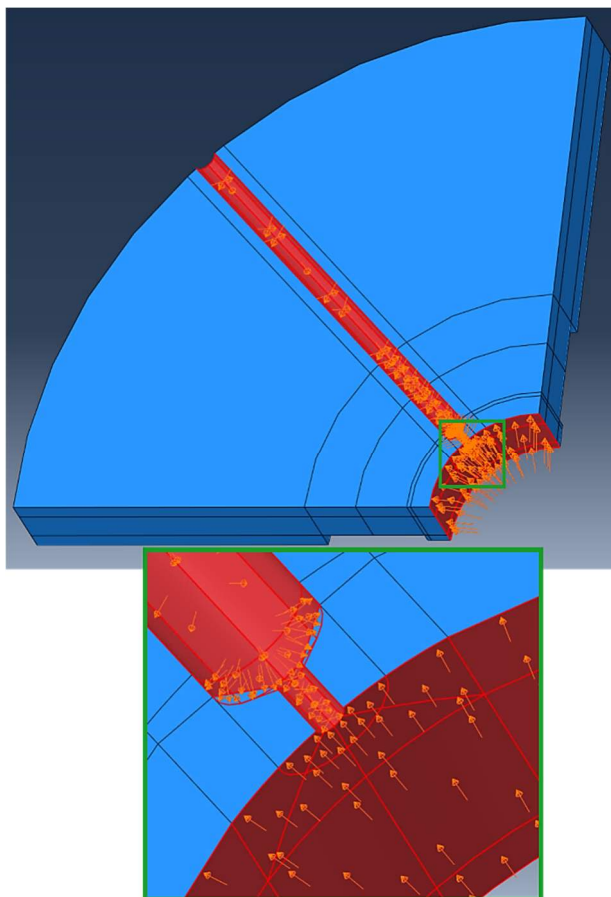


Figure 14. Structural FEA Pressure Loading.
Pressure loading is modeled along the ID of the ring and throughout the length of the port.

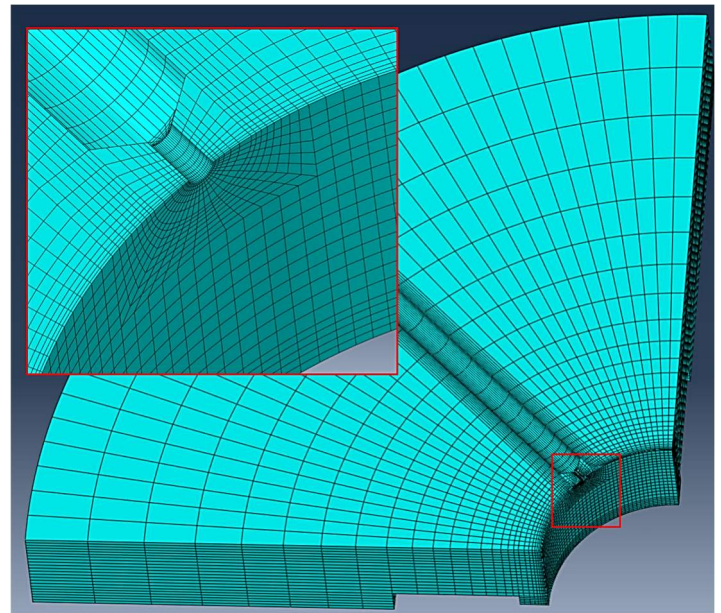


Figure 15. Un-cracked Structural FEA Mesh.
29,044 twenty-node full-integration hexahedral elements and 127,476 nodes.

2.3. FCG Analysis Set-up

The un-cracked structural FEA model was imported into the FCG software and split into GLOBAL and LOCAL models (see Figure 16). The location and size of an initial crack was specified in the LOCAL model. The LOCAL model reconnects with the GLOBAL model.

It is known that cracking initiated somewhere along the length of the smaller diameter region of the thermocouple penetration, henceforth referred to as the “step-down” in the port (marked by the red box in Figure 8). In this work, the location of crack initiation was based on the maximum principal stresses along the length of the step-down in the port of the un-cracked structural FEA model. The top of the step-down (i.e., superficial to the chamfer) had larger maximum principal stresses for nearly all of the transient than the bottom of the step-down (i.e., superficial to the ID of the ring). Thus, the location of crack initiation was assumed to occur at the top of the step-down. Crack initiation was assumed to be a 0.010 inch radius semi-circular crack. This crack was inserted into the LOCAL model (see Figure 17)

A radial fan mesh of elements around the crack tip was created in the LOCAL model. While the FCG software provides default settings when creating the radial fan mesh, the software provides the user with control over a number of the parameters (crack tube radius, number of elements radially and circumferentially around the crack tip, etc.). Initially, the crack tube radius was set to 0.001 inches, and the crack tube mesh used three crack tube rings and eight circumferential elements around the crack tip (see Figure 18). The remaining volume of the

LOCAL model was filled with ten-node tetrahedral elements. On the boundary of the LOCAL model that connects to the GLOBAL model, thirteen-node pyramid elements that are actually collapsed twenty-node hexahedral elements (where eight nodes on one face are collapsed into one node) are used to interface with the twenty-node hexahedral elements in the GLOBAL model. This produces a fully compatible mesh without the need to resort to constraint equations to tie dissimilar mesh regions together.

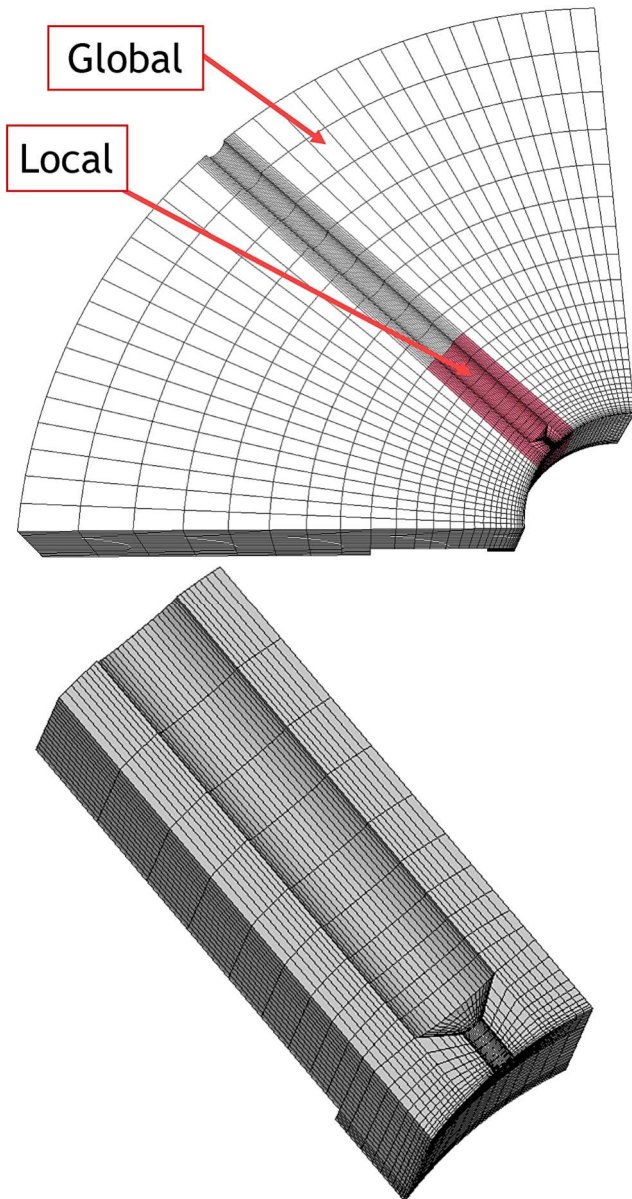


Figure 16. GLOBAL and LOCAL Model Split of the Un-cracked Structural FEA (Top) and LOCAL Model (Bottom)

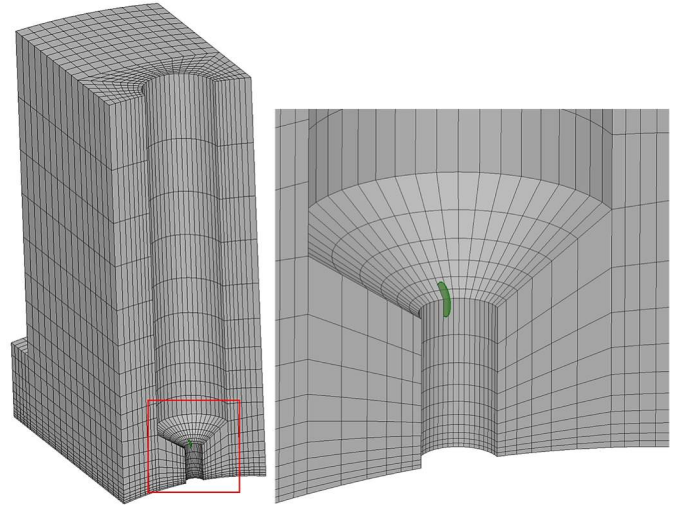


Figure 17. Location of 0.010 Inch Radius Semi-circular Crack in the LOCAL Model

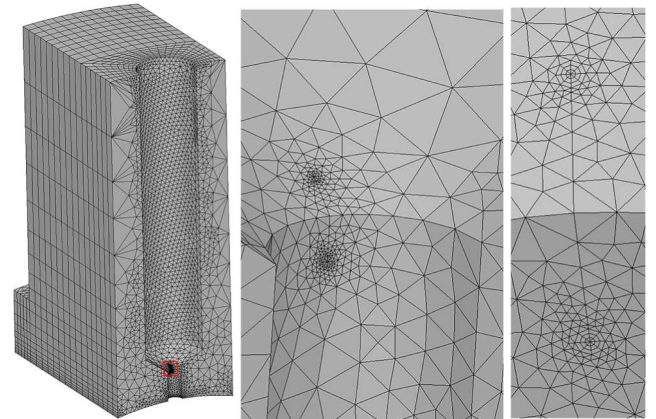


Figure 18. 0.010 Inch Radius Semi-circular Crack Mesh in the LOCAL Model.

Initially, the crack tube radius was set to be 0.001 inches and the crack tube mesh used three crack tube rings and eight circumferential elements around the crack tip.

2.4. Crack Growth Step Process

An explicit FCG analysis is an automated process that consists of iterative growth steps. Each growth step results in a new crack front. The outline of a growth step for the FCG software used in this work (Franc3D) is:

- (1) Extraction of nodal displacements from the FEA solution of the current crack mesh for all solution times in the transient (i.e., obtained from the Abaqus .odb file).
- (2) Compute stress intensity factors (K_I, K_{II}, K_{III}) for all nodes along the crack for all solution times in the transient.
- (3) Compute the stress intensity factor range (ΔK) for all nodes along the crack front using the K results from Step 2.
- (4) Grow the crack using the user specified FCG settings and the ΔK results determined in Step 3.
- (5) Re-mesh the FEA model of the current crack mesh and write the FEA model input file (i.e., the Abaqus .inp file) for the next growth step.
- (6) Solve the FEA model of the updated crack mesh using the native FEA solver (i.e., Abaqus Standard)

The thermal FEA model was solved once and the same temperature field was used in the structural FEAs of the evolving crack mesh. This removed the temperature degree of freedom from being solved in each growth step, which decreased the overall analysis computation time. This assumed that the temperature distribution was not affected by the presence of the crack. This was justified as the temperature gradient was primarily in the radial direction, which was aligned with the crack growth that was observed in the actual rings (recall Figures 4 and 8).

2.5. FCG Rate Model

A FCG rate curve for wrought austenitic stainless steels in deaerated primary water (DPW) environments was used as a starting point for the FCG rate model (see Reference [4]). The curve consists of a two piecewise Paris Law that is a function of rise time (t_{Rise}), R ratio (R), and temperature (between 212 °F and 640 °F). The most applicable FCG rate model available in the FCG software at the time of this work was a two piecewise temperature dependent Paris model (see Equation (1)).

$$\frac{Da}{DN} = \begin{cases} C_1 \cdot (\Delta K_{eff})^{n_1} & \text{for } \Delta K_{eff} < \Delta K_{eff}^* \\ C_2 \cdot (\Delta K_{eff})^{n_2} & \text{for } \Delta K_{eff} > \Delta K_{eff}^* \end{cases} \quad (1)$$

Three assumptions were made to modify the curve in Reference [4] to the same functional form as Equation (1).

(i) Although the FCG software can incorporate the Walker equation to account for R ratio effects, it was not possible at the time of this work to account for different Paris Law Model ΔK Exponents (n) in the calculation of the Walker equation. As such, the Walker equation was not used. Instead, the R ratio was set to zero. This assumption was based on a static crack analysis of the crack initiation structural FEA showing that the R ratio along the crack front was slightly negative but near zero for the transient.

(ii) Following guidance in Reference [5], the rise time was set to 77.9611 seconds based on the principal stresses at the top of the step-down in the port of the un-cracked structural FEA model.

(iii) The temperature dependence term was set to a fixed value for temperatures below 212 °F (see S_T term in Equation (2)). As temperature increases from 212 °F to 640 °F, the temperature dependence term increases in an Arrhenius fashion. A fixed value for temperatures below 212 °F results in higher FCG rates than extrapolating the original function, and thus was judged acceptable as this would promote more crack growth (which is conservative).

With these three assumptions, the FCG rate curve from Reference [3] was modified into a two piecewise temperature dependent Paris model (Equation (1)). The FCG rate model used in this analysis was:

$$\frac{Da}{DN} = C_0 \cdot (\Delta K_{eff})^n \quad (2)$$

Where,

$$C_0 = C(S_T)(S_R)(t_{Rise})^{0.227}$$

$$C = \begin{cases} 1.80 \times 10^{-24} & \Delta K_{eff} < \Delta K_{eff}^* \\ 1.59 \times 10^{-14} & \Delta K_{eff} > \Delta K_{eff}^* \end{cases}$$

$$S_T = \begin{cases} \exp\left(\frac{-4324}{T + 460}\right) & 212 \text{ °F} < T \leq 640 \text{ °F} \\ 1.61 \times 10^{-3} & T \leq 212 \text{ °F} \end{cases}$$

$$S_R = (1 - R)^{-0.559} = (1 - 0)^{-0.559} = 1$$

$$t_{Rise} = 77.9611 \text{ seconds}$$

$$n = \begin{cases} 5.08 & \Delta K_{eff} < \Delta K_{eff}^* \\ 2.46 & \Delta K_{eff} > \Delta K_{eff}^* \end{cases}$$

$\Delta K_{eff}^* = 6130 \text{ psi}\sqrt{\text{inch}}$ (Note: the intersection of the two $\frac{Da}{DN}$ curves is constant with respect to temperature)

Temperature was varied in whole-number increments from 70 °F to 640 °F in Equation (2) to generate a table of FCG rate coefficients for use in the FCG software. The threshold stress intensity factor range ($\Delta K_{threshold}$) was set to zero and the critical stress intensity factor ($K_{critical}$) was set to be very high for all temperatures so that the FCG analysis would not prematurely stop.

2.6. Crack Growth Settings

Stress intensity factors (K) were calculated using the M-integral method. The M-integral method (also called the interaction integral) is numerically very similar to the domain formulation of the J-integral. Unlike the J-integral, which only computes one scalar value representing the strain energy release rate, the M-integral uses superposition and an auxiliary crack-front solution to separate out K values for all three fracture modes (K_I , K_{II} , K_{III}) from the strain energy release rate. The M-integral method is the default setting in the FCG software to calculate K values.

The effective stress intensity factor range (ΔK_{eff}) was defined strictly as K_{max} minus K_{min} and to only consider mode one stress intensity factor (K_I). These are the default settings in the FCG software, which were kept for simplicity of the analysis. Thus, ΔK_{eff} and R were defined as:

$$\Delta K_{eff} = \Delta K_I = K_{I,max} - K_{I,min} \quad (3)$$

$$R = \frac{K_{I,min}}{K_{I,max}} \quad (4)$$

The temperature dependence was set to linearly interpolate between K_{max} and K_{min} . This was done because it cannot be known a priori whether K_{max} or K_{min} was associated with a higher or lower temperature.

The kink angle was set to be planar, forcing the crack to grow within a fixed plane. This was consistent with the crack growth that was observed in the actual rings (recall Figures 4 and 8). This was done in the interest of computational efficiency, and to be consistent with observed crack growth in the rings.

Lastly, crack face traction or contact was not defined for simplicity of the analysis. In the cases where the stresses in the vicinity of the crack front are compressive and would cause the crack faces to pass through one another, negative K_I results would be computed. This is because contact elements were not explicitly inserted between the crack faces to prevent crack face overlap. Although crack face overlap is physically unrealistic, meaningful engineering predictions can be made with these values, provided that appropriate FCG rate parameters are used.

3. RESULTS AND DISCUSSION

The median crack extension (i.e., how much the crack front changes in an average sense) and the crack tube radius was initially set to be small and increased at various times throughout the analysis to decrease the computational time. This was also done to avoid errors such as a self-intersecting crack front and crack front curve fitting errors. The FCG analysis was manually stopped at 48 growth steps, where the final crack front (growth step 48) was near the vicinity of the observed final crack front of the ring.

The FCG analysis progressed in a trial-and-error fashion over one month of full-time work. This was primarily due to the inexperience of the user and adjusting the previously discussed crack growth settings. Future similar analysis efforts by an experienced user would take less time.

The FCG software processes within a growth step (steps 1 through 5 of a growth step – see Section 2.4) used one central processing unit (CPU) and the FEA solver used 32 CPUs. A single growth step took about two hours to complete, with one hour for the FCG software processes and one hour for the FEA solver

The distribution of crack fronts that resulted from the FCG analysis in 48 growth steps can be seen in Figure 19. This figure shows the cross-section down the length of the thermocouple port. The results of the analysis (Figure 19) qualitatively matched the directional path and final flaw size seen in the DE metallographic images of the rings exceptionally well (Figure 8).

As seen in Figure 19, the crack split into two cracks near the flange of the ring. One crack continued up through the body of the ring to achieve the final crack front and the other crack continued through the flange. This was done automatically without user intervention.

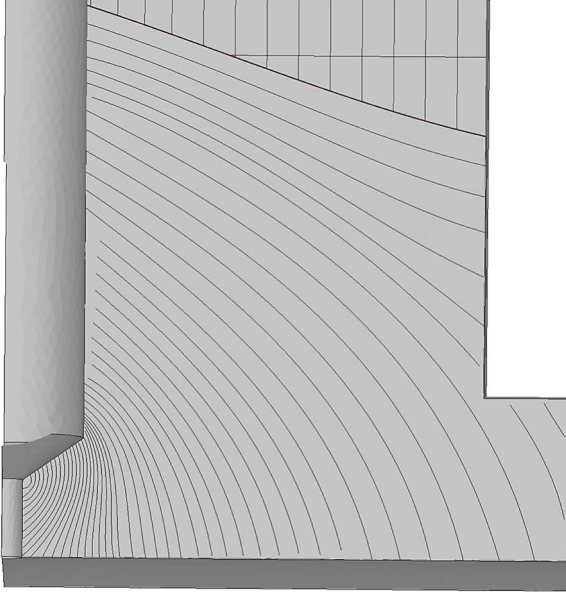


Figure 19. Cross-sectional View of the LOCAL Model and the Crack Fronts Calculated at Each Growth Step.

This is a cross-sectional section view down the length of the thermocouple port. Up to and including growth step 48 is pictured. The final crack front (at growth step 48) was near the vicinity of the observed final crack front of the ring.

The measurement data available for the rings is the surface crack length. Initially, the length of cracks along the ID of the ring was measured. Once the cracks reached the edge of the ring in the axial direction, the length of the cracks along the radial direction of the ring was measured. This data is difficult to compare to the analysis results as the crack front changed shape and grew bi-axially through the thickness of the ring. A comparison could be made between the data and the analysis results for the surface crack length along the ID of the ring. This cannot be done without an assumption of cycles to crack initiation as the analysis does not include these cycles. Although the number of cycles to crack initiation for the rings is known to be small, it is not known exactly. In References [1] and [2] the number of cycles to crack initiation was based on extrapolation of the surface crack length data. Reference [1] estimated 221 cycles (using all available data) and Reference [2] estimated 1,350 cycles (using data at 8,000 and 14,359 cycles only). As these numbers are estimates, no comparison is made in this report between the surface crack length data and the results of the analysis.

9,806 cycles were calculated to achieve the final crack size and shape (see Figure 20). This number of cycles does not include cycles to initiation and therefore is not exactly comparable to the number of the cycles the rings experienced (38,000 cycles pictured in Figure 8). Recall that the number of cycles to crack initiation for the rings is known to be small but not known exactly. As such, the 9,806 cycles calculated for FCG is a conservative estimate of the number of cycles required to reach the crack size and shape shown in Figure 8.

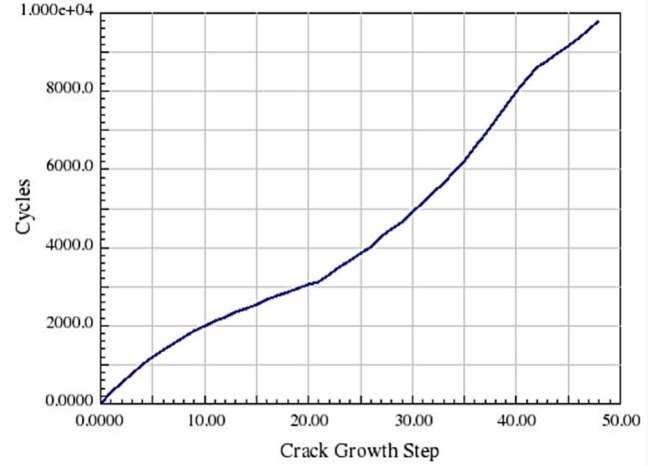


Figure 20. Cycles versus Crack Growth Step – Temperature Interpolated Between K_{max} and K_{min} . 9,806 cycles predicted to achieve final crack front.

Certain crack growth settings can be changed after a FCG analysis is completed and the number of cycles between each crack front is re-calculated. The temperature dependence setting was first changed to use the temperature at K_{min} (4,523 cycles; see Figure 21) and then to use the temperature at K_{max} (23,204 cycles; see Figure 22). This change was expected as higher FCG rates typically occur at higher temperatures, and higher temperatures were observed to occur at K_{min} rather than at K_{max} throughout the FCG analysis. It is not expected that a different initial temperature dependence setting would have changed the distribution of crack fronts in Figure 19.

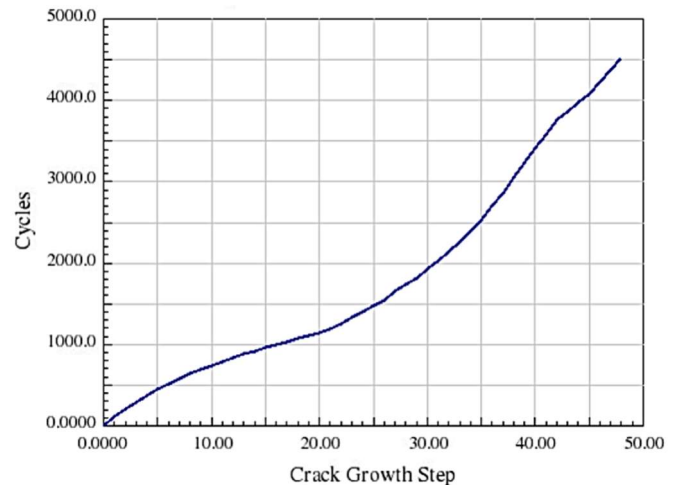


Figure 21. Cycles versus Crack Growth Step – Temperature at K_{min} . 4,523 cycles predicted to achieve final crack front.

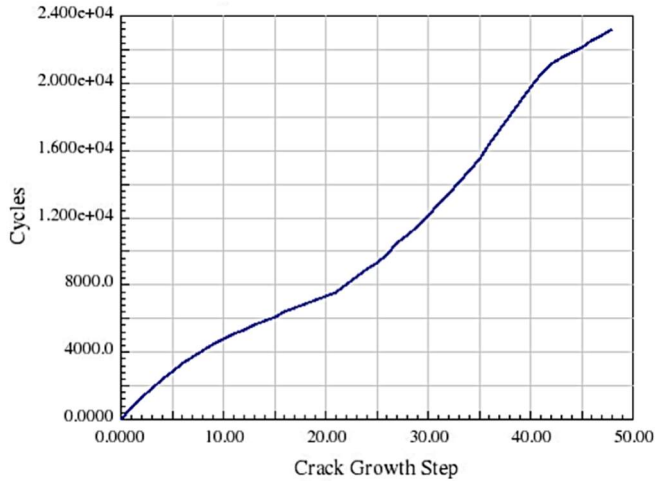


Figure 22. Cycles versus Crack Growth Step – Temperature at K_{max} .
 23,204 cycles predicted to achieve final crack front.

The R ratio was shown to straddle zero for all points along the crack front for all growth steps in the FCG analysis. The plots for R ratio for crack growth steps zero (crack initiation) and 48 (final crack front) are shown in Figures 23 and 24, respectively. This supports assumption (i) of R ratio being set to zero for the FGC rate model. This also supports the simplification of no crack face contact as $K_{I,min}$ was small compared to $K_{I,max}$.

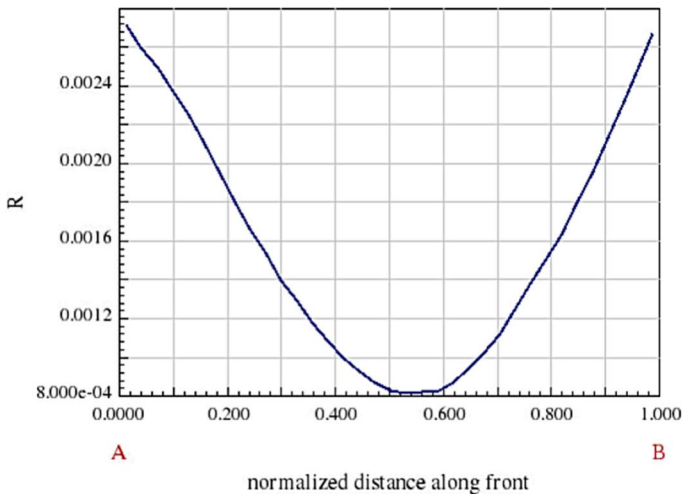


Figure 23. R Ratio versus Normalized Distance Along the Crack Front – Growth Step Zero (Crack Initiation).
 Point B is on the smaller diameter region of the penetration (i.e., the step-down).

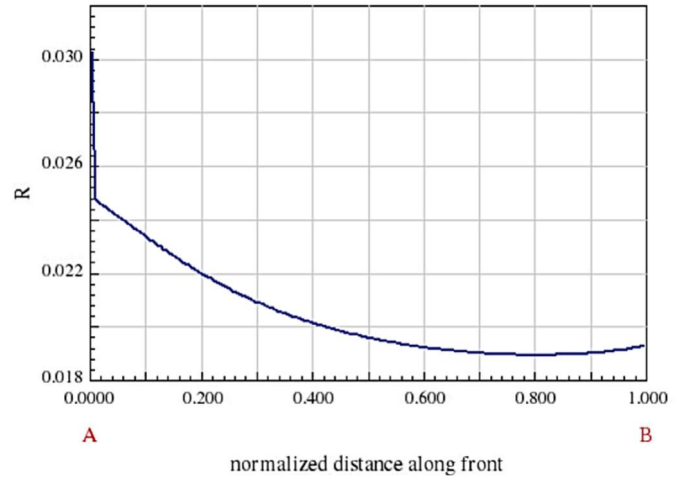


Figure 24. R Ratio versus Normalized Distance Along the Crack Front – Growth Step 48 (Final Crack Front).
 Point B is on the right side of the crack (the external surface of the ring).

Plots for ΔK for crack growth steps zero (crack initiation) and 48 (final crack front) are shown in Figures 25 and 26, respectively. The data set supporting the original curve in Reference [4] has an upper bound on ΔK of $41.9 \text{ ksi}\sqrt{\text{in}}$. As seen in Figure 25 (for the initial crack), the distribution of ΔK along the crack front has a maximum value of about $39 \text{ ksi}\sqrt{\text{in}}$. The distribution of ΔK along the crack front was partially above the $41.9 \text{ ksi}\sqrt{\text{in}}$ upper bound within a few growth steps, and was mostly above the $41.9 \text{ ksi}\sqrt{\text{in}}$ upper bound by the end of the analysis in growth step 48 (see Figure 26). This uncertainty in the FCG analysis associated with ΔK values along the crack front falling outside of the defined bounds of the available FCG rate dataset is noted.

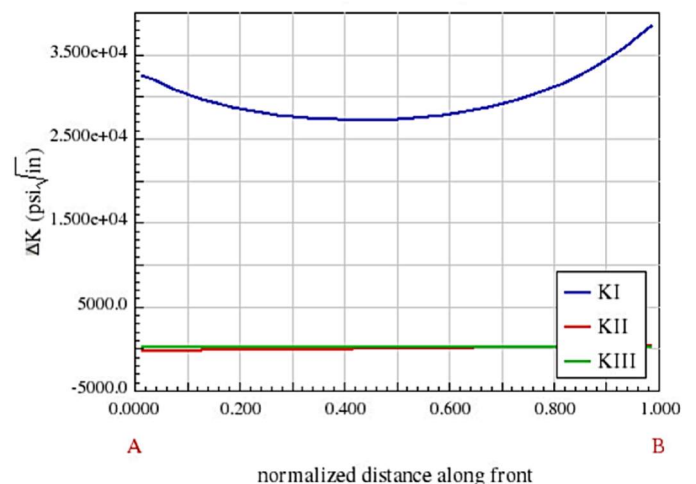


Figure 25. ΔK versus Normalized Distance Along the Crack Front – Growth Step Zero (Crack Initiation).
 Point B is on the smaller diameter region of the penetration (i.e., the step-down).

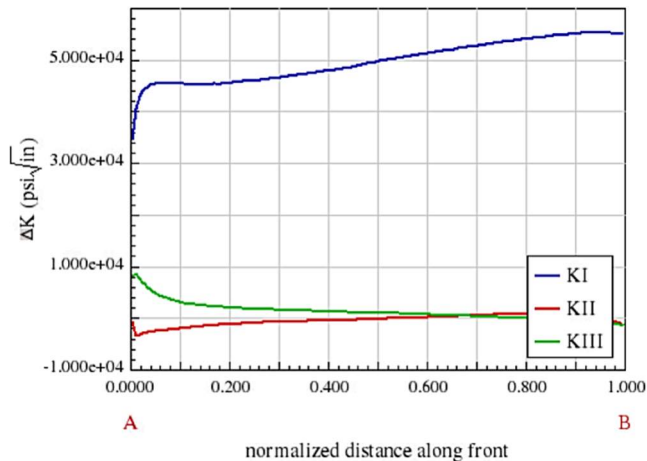


Figure 26. ΔK versus Normalized Distance Along the Crack Front – Growth Step 48 (Final Crack Front). Point B is on the right side of the crack (the external surface of the ring).

4. CONCLUSION

This work indicates that an explicit FCG analysis can provide meaningful crack front distribution results for a non-trivial thermal fatigue problem. The analysis was completed in mostly an automated fashion, where trial-and-error by the user would slow down progress. Although this analysis took about one month of full-time work, future similar analysis efforts by an experienced user would take less time.

The FCG rate model used in this work required various simplifying assumptions to be made to the FCG rate curve so that it could be accommodated in the FCG software; this may have affected the calculated number of cycles. Ideally, the full functional forms of a FCG rate model should be programmed into a FCG software. Analysis assumptions and results should be checked against defined bounds of FCG rate models.

The rise time was set to be fixed for all growth steps based on the principal stresses of the un-cracked structural FEA. Consideration should be given to adjusting the rise time value throughout the FCG analysis, and determining how rise time should be calculated using a K based method instead of a stress based method (which was consistent with the Reference [5] methodology).

The temperature dependence settings were linearly interpolated between K_{max} and K_{min} . Consideration should be given to compute FCG properties on a temperature based criteria instead of a K based criteria. In other words, use the minimum or maximum (or somewhere in between) temperature during the transient for each point along the crack front when calculating FCG properties. Although it was initially thought that using the temperature at K_{max} would provide the most conservative number of cycles, the opposite occurred in this analysis as higher temperatures were observed to occur at K_{min} rather than at K_{max} throughout the FCG analysis.

Crack face traction or contact was not defined in this analysis. Since the R ratio straddled zero for all growth steps, not including these effects was appropriate. Future similar efforts should consider including crack face traction or contact for a more representative analysis.

ACKNOWLEDGEMENTS

The analysis presented in this report was performed under a U.S. Department of Energy contract with Fluor Marine Propulsion, LLC for the Naval Nuclear Laboratory. The authors would like to acknowledge Robert D. Reinheimer for providing information on the testing and Roland S. Piehler for his input on previous analysis work.

REFERENCES

- [1] Damiani, T.M., Holliday, J.E., Zechmeister, M.J., Reinheimer, R.D., Jones D.P., “Thermal Fatigue Testing and Analysis of a thick Perforated Ring”, PVP2007-26364, Proceedings of PVP2007, 2007 ASME Pressure Vessels and Piping Division Conference, July 22-26, 2007, San Antonio, Texas.
- [2] Piehler, R.S., Damiani, T.M., “Fatigue and Crack Growth Analysis of a Thick Instrumentation Ring Subjected to Thermal Fatigue Cycling”, PVP2008-61174, Proceedings of PVP2008, 2008 ASME Pressure Vessels and Piping Division Conference, July 27-31, 2008, Chicago, Illinois, USA.
- [3] Todreas, N.E., Kazimi, M.S., “Nuclear Systems; Volume 1; Thermal Hydraulic Fundamentals”, 2nd Edition – Revised Printing, April 27, 2015.
- [4] Barron, K.C., Paraventi, D.J., “An Environmentally Enhanced Fatigue Crack Growth Model for Type 304 Austenitic Stainless Steels in Pressurized Water Reactor Environments”, PVP2021-65973, Proceedings of the ASME 2021 Pressure Vessels & Piping Division Conference, PVP2021, July 13-15, 2021, Virtual, Online.
- [5] 2015 ASME Boiler and Pressure Vessel Code, Section XI, Division 1, Case N-809, “Reference Fatigue Crack Growth Rate Curves for Austenitic Stainless Steels in Pressurized Water Reactor Environments”, Approval Date June 23, 2015.